

## Mapping of aeolian deposits of an industrial site in the arid region using the TIR bands of ASTER and study of physicochemical characters and stabilization of sand erosion

Rajendran Sankaran, Nabil Zouari, Fadhil N. Sadooni, Zulfa Ali Al Disi, Abdulaziz Al-Jabri & Hamad Al-Saad Al-Kuwari

To cite this article: Rajendran Sankaran, Nabil Zouari, Fadhil N. Sadooni, Zulfa Ali Al Disi, Abdulaziz Al-Jabri & Hamad Al-Saad Al-Kuwari (2022) Mapping of aeolian deposits of an industrial site in the arid region using the TIR bands of ASTER and study of physicochemical characters and stabilization of sand erosion, *Geomatics, Natural Hazards and Risk*, 13:1, 2535-2559, DOI: [10.1080/19475705.2022.2122873](https://doi.org/10.1080/19475705.2022.2122873)

To link to this article: <https://doi.org/10.1080/19475705.2022.2122873>



© 2022 The Author(s). Published by Informa UK Limited, trading as Taylor & Francis Group.



[View supplementary material](#)



Published online: 13 Sep 2022.



[Submit your article to this journal](#)



Article views: 256



[View related articles](#)



[View Crossmark data](#)

# Mapping of aeolian deposits of an industrial site in the arid region using the TIR bands of ASTER and study of physicochemical characters and stabilization of sand erosion

Rajendran Sankaran<sup>a</sup> , Nabil Zouari<sup>b</sup>, Fadhil N. Sadooni<sup>a</sup> , Zulfa Ali Al Disi<sup>b</sup>, Abdulaziz Al-Jabri<sup>c</sup> and Hamad Al-Saad Al-Kuwari<sup>a</sup> 

<sup>a</sup>Environmental Science Center, Qatar University, Doha, Qatar; <sup>b</sup>Environmental Science Program, Department of Biological and Environmental Sciences, College of Arts and Sciences, Qatar University, Doha, Qatar; <sup>c</sup>Qatar Fertiliser Company (QAFCO), Mesaieed, Qatar

## ABSTRACT

This study describes the spectral emissive character of silicate and carbonate minerals of aeolian deposits and maps the deposits and sand encroachments that occurred in and around the site 5/6 of Qatar Fertilizer Company (QAFCO), Qatar using thermal infrared (TIR) bands of ASTER. The results of studies show that the quartz and unaltered silicates have spectral features between 8.12 and 9.27  $\mu\text{m}$ , and the calcite and dolomite have emissivity minima near 11.4 and 11.2  $\mu\text{m}$ , respectively. The mapping of deposits, dunes, and carbonate formations using the bands, and quartz index (QI), and carbonate index (CI) displayed their occurrence, distribution, and direction of sand movement from NW to SE. The sand encroachment was mapped using high spatial resolution satellite data of WorldView-2. The study of physicochemical characteristics of field samples showed the occurrence of sand grains up to 99.81% and the XRD and geochemical analyses represented the presence of quartz, calcite, dolomite, albite, and halite minerals in the deposits. In addition, the bacterial strains isolated from the samples indicated high urease activity leading to precipitation of carbonate minerals via microbially induced calcite precipitation (MICP) processes, and demonstrated high potential for utilization for sand stabilization of the QAFCO site.

## ARTICLE HISTORY

Received 22 November 2021  
Accepted 6 September 2022

## KEYWORDS

Aeolian deposits; ASTER indices; TIR bands; physicochemical characters; sand stabilization; Qatar

## 1. Introduction

Aeolian processes produce vast areas of sand and dunes in the arid region and need to monitor since they frequently exceed desertification or encroaching land and degrading infrastructures of industries (Gómez et al. 2018; Sur and Chauhan 2019;

**CONTACT** Rajendran Sankaran  [srajendran@qu.edu.qa](mailto:srajendran@qu.edu.qa)

 Supplemental data for this article can be accessed online at <https://doi.org/10.1080/19475705.2022.2122873>.

© 2022 The Author(s). Published by Informa UK Limited, trading as Taylor & Francis Group.

This is an Open Access article distributed under the terms of the Creative Commons Attribution License (<http://creativecommons.org/licenses/by/4.0/>), which permits unrestricted use, distribution, and reproduction in any medium, provided the original work is properly cited.

Aydda et al. 2020, 2019; Delgado Blasco et al. 2020; Wen et al. 2020; Karanisa et al. 2021). Studies have proven that remote sensing techniques help to map and monitor the sand deposits and sand movements, measure migration rates of dunes and the direction of the movement of dunes, and assess the areas of sand encroachments (Crósta et al. 2003; Rowan et al. 2003; Amer et al. 2010; Engel et al. 2018; Qiu et al. 2019; Song et al. 2019; Zhao et al. 2019; Aydda et al. 2020; Delgado Blasco et al. 2020). Satellite data acquired in the visible, near-infrared, and shortwave infrared spectral regions (0.4–2.5  $\mu\text{m}$ ) have been widely utilized to map and study the different resources of the Earth's surface (Hunt et al. 1973; Clark et al. 1990) but, the spectral regions are useless for detecting quartz mineral that is present in the sand deposits and dunes. Because the quartz does not show spectral features in those spectral regions and exhibits a strong doublet emissivity feature in the longwave infrared (LWIR) spectral region. The 8–14  $\mu\text{m}$  (LWIR) is suitable for the identification and quantification of aeolian quartz minerals and mapping of sand deposits and dunes (Vaughan et al. 2003; Eisele et al. 2015). The image processing methods include the principal component analysis (PCA) (Chavez and MacKinnon 1994), Maximum Likelihood (ML) classification (Julien et al. 2011; Hogland et al. 2013), and NDVI (Normalized Difference Vegetation Index) (Levin et al. 2006) are utilized to map such aeolian deposits.

Mapping of sand deposits and dunes was carried out using ASTER minerals indices (Ninomiya 2002; Ninomiya et al. 2005; Rockwell and Hofstra 2008; Corrie et al. 2010). The spectral indices are defined for discriminating various surface minerals and mapping lithologies, since the indices work on predefined transform factors and there is a possibility of identifying minerals from the resultant images (Crist and Cicone 1984; Yamaguchi and Naito 2003). Using the SWIR and TIR electromagnetic wavelengths, the indices have been defined by various investigators for the discrimination of various minerals and lithologies (Ninomiya 2002; Ninomiya et al. 2005; Corrie et al. 2010). To measure the migrations of dunes and assess the desertification and land degradation, the applications of the data of Landsat (Pradhan et al. 2018; Baird et al. 2019), SPOT (Satellite Pour l'Observation de la Terre) (Engel et al. 2018), ASTER (Advanced Spaceborne Thermal Emission and Reflection Radiometer) (Ninomiya et al. 2005; Corrie et al. 2010; Cudahy et al. 2016; Rajendran et al. 2020, 2011), Quickbird (Hesse 2009), SRTM (Shuttle Radar Topography Mission) (Afrasinei et al. 2018), Sentinel (Gómez et al. 2018) and LiDAR (Light Detection and Ranging) (Wolfe and Hugenholtz 2009) are well demonstrated. But, meager attempts have been made to map the sand deposits and sand encroachments of industrial areas using satellite data. Studies are also required urgently for the stabilization of sand of the industrial sites to stop sand erosion around the sites and protect the infrastructures of the industries from the hazards. Recently, Al-Disi et al. (2016) characterized the extracellular polymeric substances (EPS) of *Virgibacillus* strains in the soil and sand which are capable of forming a high Mg-calcite and protodolomite to stabilize the soil and sand. Bibi et al. (2018) isolated, differentiated, and tested the biodiversity of ureolytic bacteria in Qatari soil and demonstrated the potential of microbially induced calcite precipitation (MICP) for soil stabilization. Studies were

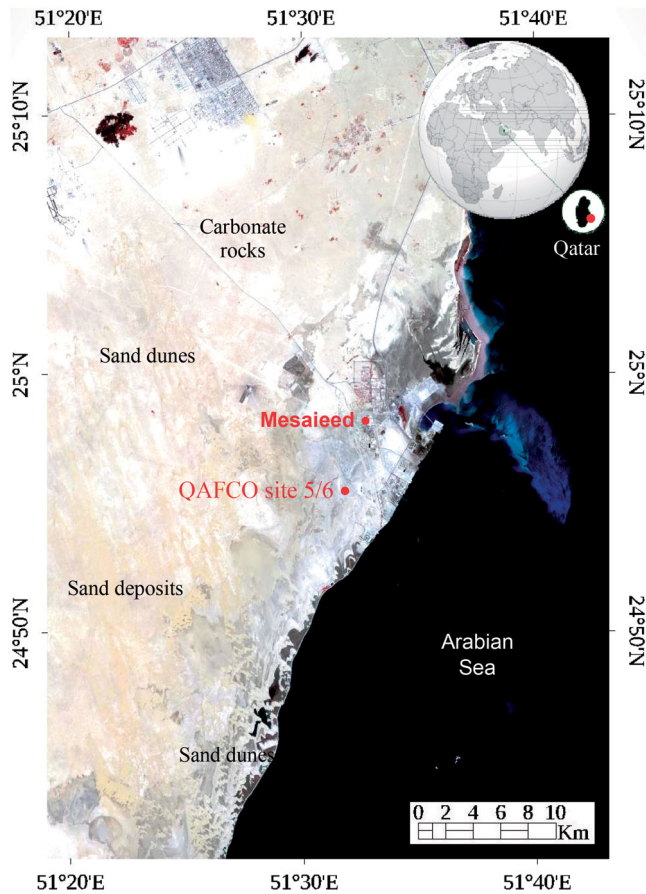


**Figure 1.** ASTER image (R:3; G:2; B:1) showing the occurrence and spatial distribution of sand deposits and the location of QAFCO site 5/6.

carried out in the laboratory for the biophysicochemical improvement of desert sand to reduce sand erodibility using various organic or inorganic compounds (Weiner and Dove 2003; Li et al. 2007, 2003, 2000; Wang et al. 2018; Xu et al. 2018; Zhang et al. 2019, 2013).

Therefore, this study aims to map the sand deposits and sand encroachments that occurred in and around the Qatar Fertiliser Company (QAFCO) of the State of Qatar using ASTER data and attempts to stabilize the sands on the laboratory scale. This study utilizes the five TIR bands of ASTER since the bands can be well utilized to map minerals such as quartz and feldspar and sand deposits and dunes (Hunt and Salisbury 1974, 1975, 1976; Crósta et al. 2003; Rowan et al. 2003; Amer et al. 2010; Gabr et al. 2010). Quartz provides emissivity minima in the ASTER bands 10 and 12 and shows high emissivity in the spectral bands 11, 13, and 14 (Ninomiya 2002; Ninomiya et al. 2005). The data products are available at no cost from April 2016 (<https://lpdaac.usgs.gov/news/aster-data-available-at-no-charge/>). Thus, the objectives of the study are 1) to describe the spectral absorptions of quartz and carbonate

**Table 1.** Showing the coordinates of samples collection in the QAFCO site 5/6.

Sample no.	Coordinates		Quantity	Remarks
	Latitude	Longitude		
S1	24°55'27.47"N	51°32'14.94"E	10 Kg	Sand deposit near NS Fence
S2	24°55'45.53"N	51°32'8.28"E	10 Kg	Sand deposit at the corner of NS-EW Fences
S3	24°55'47.99"N	51°32'16.22"E	12 Kg	Sand deposit samples near EW Fence
S4	24°55'52.23"N	51°32'29.32"E	10 Kg	Sand deposit samples near EW Fence
S5	24°55'48.16"N	51°32'29.88"E	12 Kg	Sand deposit in water channel/trench behind site 6
S6	24°55'23.01"N	51°32'34.29"E	12 Kg	Soil/Sabkha sample front to site 5

minerals, 2) to discriminate and map the sand deposits and dunes that occurred in and around the Qatar Fertiliser Company (QAFCO) site 5/6, the State of Qatar using the TIR bands of the ASTER and quartz and carbonate indices, 3) to characterizes the physicochemical characters of the sand and 4) to experiments the stabilization of the sand by bacteria method at laboratory scale to understand the occurrence and spatial distribution of the sand deposits and dunes of the study site and protect the industry from the sand deposit and sand encroachment hazards. The study also maps areas that are vulnerable to sand deposits and encroachments using WorldView-2 data.

## 2. QAFCO site 5/6

The area of study covers and around the site of Qatar Fertiliser Company (QAFCO) 5/6 (Figure 1). It is situated on the east coast of the State of Qatar, below the Mesaieed Port, at a distance of 9 km from Mesaieed town and 35 km from the Hamad International Airport. The area is experiencing high summer temperatures, low rainfall, and low humidity which contribute to high rates of evaporation in the area. The area in and around the site is deposited by carbonate rocks of the Dammam Formation at the base and overlain by the limestone, dolomite, and evaporite rocks of the Miocene Dam Formation that is 40–80 m thick. The Dammam formation was deposited during the period of Lower-Middle Eocene and divided into lower and upper parts in Qatar. The lower formation consists of about 12 m of compact, fossiliferous, chalky limestone with laminated fossiliferous shale. Whereas, the upper formation ranges in thickness between 10–65 m and is composed of dolomitic limestone (Hamad 2005). Quaternary deposits have occurred as sabkhas, and unconsolidated sediments such as fine-grained alluvium, aeolian sand, and beach deposits in coastal areas. The sand deposits and encroachment by sand movement on the industry site are high and a detailed study to map and mitigate this phenomenon is important.

## 3. Data and methods

### 3.1. ASTER data and image processing

In this study, the thermal infrared (TIR) bands of ASTER having 90 m spatial resolution were used to map the sand deposits and dunes, and the areas that are vulnerable to sand encroachment and land degradation were mapped using Worldview-2

data having 0.5 m resolution. ASTER has three bands in the visible near-infrared (VNIR), six in the shortwave infrared (SWIR), and five bands in the thermal infrared (TIR) wavelength regions, and the bands have 15 m, 30 m, and 90 m spatial resolutions respectively (Fujisada 1995). Here, a cloud-free ASTER Level 1T (L-1T) spectral bands dated 31 May 2005 were obtained from NASA Land Processes Distributed Active Archive Center User Services, USGS Earth Resources Observation and Science (EROS) Center (<https://LPDAAC.usgs.gov>). The data had less than 2% cloud cover and the registration of imageries was carried out using the GCPs. The radiometric, geometric, and atmospheric corrections of the data were carried out using FLAASH (Fast Line-of-sight Atmospheric Analysis of Spectral Hypercubes) in Envi 5.5 software (<https://www.harrisgeospatial.com>) after a correction for cross-track illumination to remove the water vapor and aerosols effects that found on the data. The sensor characters of the ASTER and Worldview-2 are given in Table 1 in the supplementary material.

As discussed above, the ASTER minerals indices are used for discriminating between various surface minerals and mapping lithologies (Crist and Cicone 1984; Ninomiya 2002; Yamaguchi and Naito 2003; Ninomiya et al. 2005; Corrie et al. 2010). This study uses the carbonate index (CI) and quartz index (QI) of Ninomiya (2002) and Ninomiya et al. (2005) to map the sand deposits and dunes of the study site since the indices were developed using the suitable spectral bands of ASTER and well demonstrated to map quartz and carbonate minerals of similar regions (Rockwell and Hofstra 2008; Corrie et al. 2010). Ninomiya (2002) and Ninomiya et al. (2005) described the ASTER minerals indices as below.

$$\text{Quartz Index (QI)} = (\text{Band11}) \times (\text{Band11}) / (\text{Band10}) \times (\text{Band12})$$

where QI is expected to be high for quartz and other siliceous rocks, but low for potassium feldspar, and gypsum (Ninomiya 2002; Ninomiya et al. 2005). Quartz ( $\text{SiO}_2$ ) displays a characteristic spectral feature between ASTER bands 10–12 in the thermal infrared region and found that emissivity is higher at ASTER band 11 compared to bands 10 and 12.

$$\text{Carbonate Index (CI)} = \text{Band13} / \text{Band 14}$$

where CI is expected to be high for the carbonate minerals such as calcite and dolomite, but the index is not expected to identify other carbonate rocks (Ninomiya 2002; Ninomiya et al. 2005). Carbonate minerals such as calcite and dolomite and bearing limestones and dolomites have a unique spectral absorption feature in ASTER band 14. Based on differences in the spectral emissivity between bands 13 and 14, the CI is defined. The spectral emissivity of quartz and carbonate minerals are described in Sec. 4.1.

### **3.2. Assessment of the vulnerability of sand encroachment**

The vulnerability to sand encroachment on the industrial site was assessed using the high spatial resolution (0.5 m) data of WorldView-2 acquired on February 16, 2021. Previous studies have shown that the application of false-color composites is well utilized to monitor aeolian dunes (Runnström 2003; Hugenholtz et al. 2012; Ahmady-

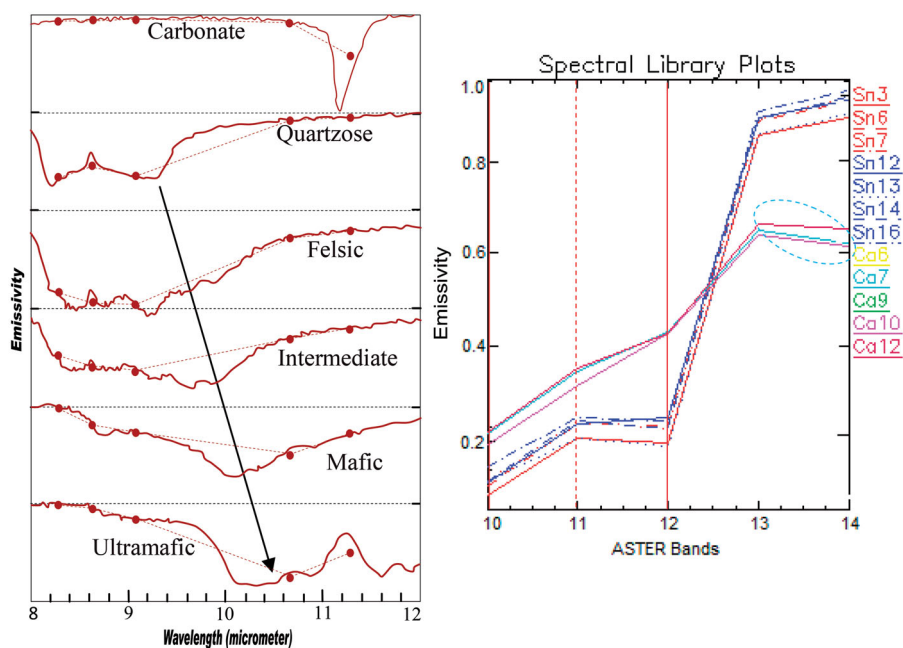


**Figure 2.** (a) Emissivity spectra of carbonate, quartzose, granite, diorite, gabbro, peridotite rocks with the convolved data to ASTER TIR band passes. Each tick on Y-axis registers 1.0/0.75 in emissivity except for (b): 1.0/0.5 (after Ninomiya et al. 2005) and (b) ASTER TIR bands image spectra of sand deposits (Sn3 to Sn16) and carbonate rocks (Ca6 to Ca12) of QAFCO region (see Figure 3 for the locations of the image spectra).

Birgani et al. 2017). In this study, an RGB image was developed to assess the vulnerability of sand encroachment (Gómez et al. 2018; Bullard and White 2002). The images were compared visually against the results of ASTER to study the sand advance. From which, the areas vulnerable to sand encroachment and degraded lands are assessed (Fichera et al. 2012; Allbed and Kumar 2013; Vacca et al. 2014; Allbed et al. 2014a, 2014b; Vogiatzakis and Melis 2015).

### 3.3. Field and laboratory studies

Satellite data results were verified in the field by conducting fieldwork during April 2021 and validated the occurrence and distribution of the sand deposits, dunes, and sand encroachment. Representative sand samples having 10–12 kg. were collected from the field and physicochemical characteristics of the samples are studied at the laboratory of the Environmental Science Center, Qatar University. The analyses of grain sizes using a Master sizer 3000 instruments were carried out to understand the grain sizes distribution in the sand deposits. The concentration of major elements, including the concentration of Si, CO<sub>3</sub>, SO<sub>4</sub>, PO<sub>4</sub>, and Cl using ICP-MS were carried out to assess the chemistry of the sand deposits. The samples were used to study the major minerals of the deposits by the X-Ray diffraction method at the Center for Advanced Materials, Qatar University.

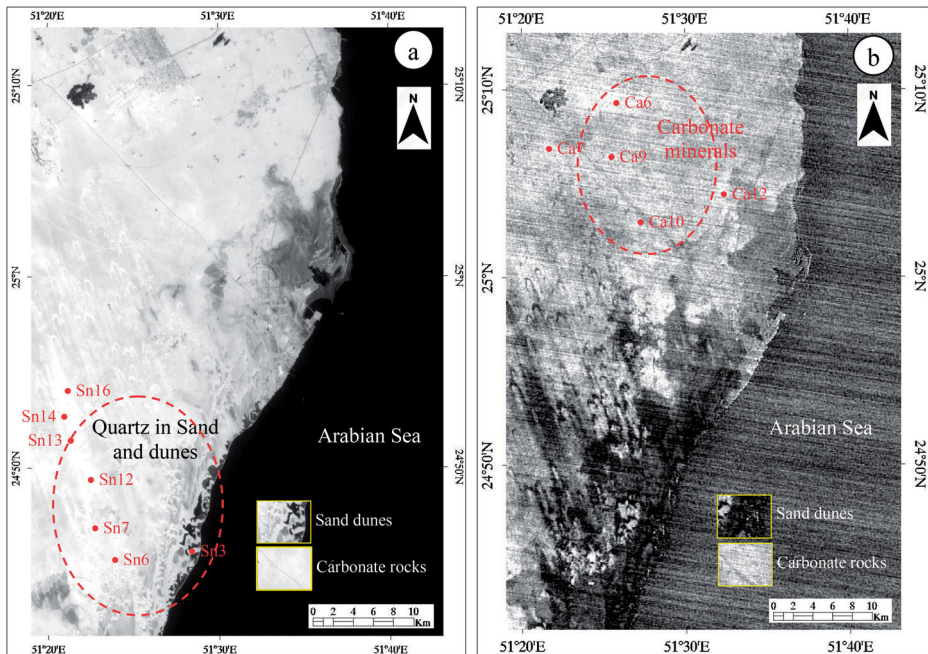


**Figure 3.** (a) Quartz index (QI), and (b) Carbonate index (CI) images show the occurrence of quartz and carbonate minerals as bright features. Locations represent the sites of image spectra collected over sand deposits and carbonate rocks.

### 3.4. Stabilization of aeolian sand

In addition to the above, the samples were studied for sand stabilization using isolated ureolytic bacteria strains at the Department of Biology and Environmental Microbiology, Qatar University. The isolation of ureolytic bacterial strains by adding 2 g of each soil sample to 20 ml of urea culture media. The cultures were incubated for 72 h in a shaker set at 30 °C and 200 rpm. Then, 3 successive enrichment cultures were performed using the initial culture: 2 ml per 20 ml. For the purification of the ureolytic bacterial strains, the strains were performed using the streak plate method until pure strains were obtained. The identification of the bacterial strains was performed by matrix-assisted laser desorption ionization-time of flight mass spectrometry (MALDI-TOF MS). The determination of bacterial growth and urease activity was studied from the cultures performed using 20 g L<sup>-1</sup> urea after 3 days of incubation using the phenol-hypochlorite method as described by Burbank et al. (2012) and Bibi et al. (2018). Further, the strains were inoculated in urea media supplemented with calcium chloride, and then incubated in a shaker set at 200 rpm and 30 °C for 5 days. At the end of the incubation period the precipitations were obtained by centrifugation at 5000 rpm for 10 min. The recovered precipitates were washed three times with distilled water to remove any residuals before air drying at 40 °C. The characterization of minerals formed by the isolates was studied using X-Ray diffraction (XRD) analyses.

## 4. Results

### 4.1. Spectral emissivity of sands and dunes

Figure 2(a) shows the spectra of different rocks that were measured using a portable thermal infrared Fourier Transform Interferometer manufactured by Design and Prototypes, Ltd. (Hook et al. 1992; <http://www.dpinstruments.com/>) and convolved into the responsivity functions of ASTER-TIR bands (Fujisada 1995). The plot shows the direction of emissivity against the spectral properties of selected rocks (after Ninomiya and Fu 2003; Ninomiya et al. 2005). The spectra of carbonate rock exhibit emissivity minima in ASTER band 14 (near 11.4  $\mu\text{m}$  for calcite and 11.2  $\mu\text{m}$  for dolomite) due to the C–O bending mode (Figure 2a; Table 1(a) in supplementary material). Quartz and unaltered igneous rocks (consisting of silicate minerals) do not show any spectral features in VNIR to SWIR, in contrast, they have prominent spectral features in the TIR region due to fundamental asymmetric Si–O–Si stretching vibrations. Quartz in quartzose and felsic rocks shows absorption features (i.e. emissivity minima) in the ASTER bands 10 and 12 and a relatively high emissivity in band 11 when compared with the bands 10 and 12 (Figure 2a; Table 1(a) in supplementary material). Studies show that the ratio of emissivity at band 12 to band 13 for silicate rocks (typically igneous rocks) increases when the  $\text{SiO}_2$  content decreases (i.e. as the rock type changes from felsic to mafic) as shown in Figure 2(a) (see the direction of the arrow). The image spectra of sand deposits and carbonate rocks of the QAFCO region collected over the image developed using the TIR bands of ASTER are given in Figure 2(b). The plot shows that the spectra of sand deposits (Sn3 to Sn16 in Figure 2b) exhibit the emissivity minima in the bands 10 and 12 (solid red vertical lines) with a relative high emissivity in the band 11 (dashed red vertical line) as studied. Also, the image spectra of carbonate rocks (Ca6 to Ca12 in Figure 2b) shows the emissivity minima in the ASTER band 14 (blue elliptical). Since the quartz exhibits emissivity (minima) in the ASTER bands 10 and 12 and high emissivity in the bands 11, 13, and 14 and carbonates show emissivity minima in band 14, the bands used in the quartz index and carbonate index can be well utilized to map the sand deposits and carbonate rocks of the QAFCO region (Figure 2; Ninomiya 2002; Ninomiya et al. 2005; Corrie et al. 2010; Rajendran et al. 2011).

### 4.2. Mapping of sand and dunes

Among the VNIR, SWIR, and TIR spectral bands of ASTER, the three VNIR bands have important sources of information for transition metals, especially iron and some rare-earth elements (REE) (Rowan et al. 1986), and chlorophyll absorption in photosynthesizing vegetation (Knipling 1970). An increase of six bands in the SWIR region (one spectral band for Landsat vs. six spectral bands for ASTER) enhances the surface lithological mapping capability related to many silicates, carbonates, hydrates, and hydroxide minerals and can display molecular absorption features by overtones and combination of tones (Hunt 1977). As well, the five spectral bands in the TIR region provide surface temperature and emissivity, and

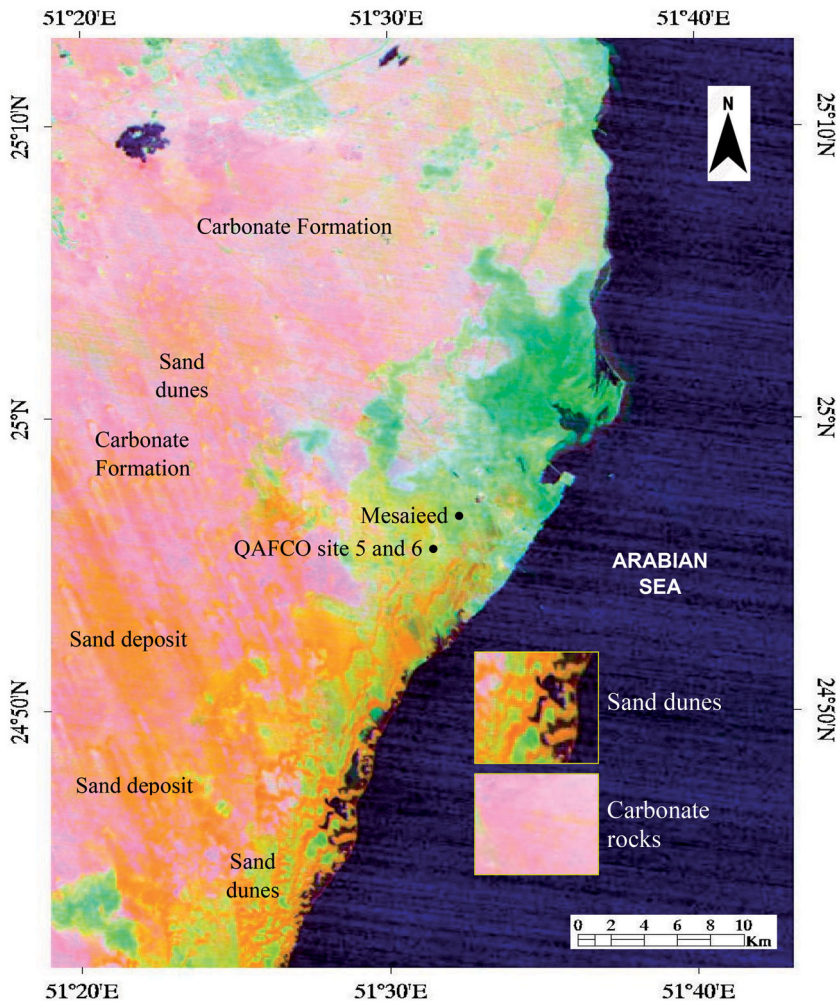


**Figure 4.** False-color composite (R: Band 6; G: Quartz index; B: CI index) showing the occurrence and distribution of sand deposits, dunes and carbonate formations in the east coast transect of the State of Qatar.

the bands can be used to map the important rock-forming minerals such as quartz and feldspar and are well utilized for mapping sand deposits and dunes (Hunt and Salisbury 1974, 1975, 1976; Crósta et al. 2003; Rowan et al. 2003; Amer et al. 2010; Gabr et al. 2010).

The interpretation of images of the ASTER bands 10 to 14 showed the occurrence of sand deposits in black in the bands 10 to 12 and white in the bands 13 and 14. The emissivity minima were observed in bands 10 and 12 when compared to band 11. The carbonate rocks (dolomites and limestones) that are associated with the sand deposits appear gray to black in all the bands; however, the rocks indicated low emissivity (absorption) in band 14. Thus, the occurrence of sand deposits and carbonate rocks in the study region was studied using the quart index (QI) and carbonate index (CI). [Figure 3](#) shows the images of the indices which exhibit the sand deposits in

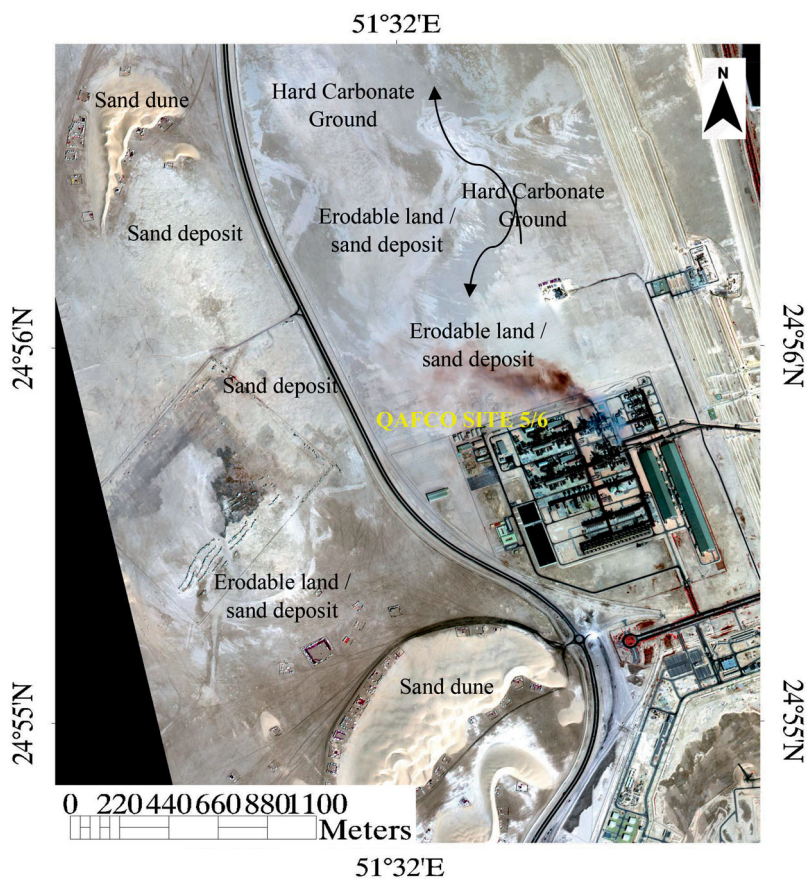


**Figure 5.** WorldView-2 satellite image acquired on February 16, 2021 showing the sand deposits in and around the QAFCO site 5/6.

bright over the QI image (red dashed circle in [Figure 3\(a\)](#), zoom to see the dunes). The carbonate rocks appear in bright over the CI image (red dashed circle in [Figure 3b](#)). The occurrence and spatial distribution of the deposits and carbonate rocks can be compared with the false-color composite (FCC) developed using the reflective spectral band 6 and, quartz and carbonate indices ([Figure 4](#)). The FCC image shows the occurrence and distribution of sand deposits and dunes in bright yellow and carbonate formation in a mixture of pink around the QAFCO site 5/6. Further, the study on the mapping of the sand deposits to the entire State of Qatar exhibited that the site is not situated at places where the windblown and sand deposits are high ([Figure 1](#) in [supplementary material](#), compare with [Figure 4](#)). The interpretation of the image ([Figure 1](#) in [supplementary material](#)) depicts that the sand deposits around the site are from land in the NW-SE direction which can be assessed from the digital elevation model (DEM) of Qatar and wind patterns that occurred over the Gulf region (Notaro et al. 2015; Peng et al. 2016; Yu et al. 2016; Aboobacker et al. 2021; Bilal et al. 2021). A study carried out using data from Copernicus Global DEM 30 m (<https://portal.opentopography.org/datasets>) for the study region confirmed further

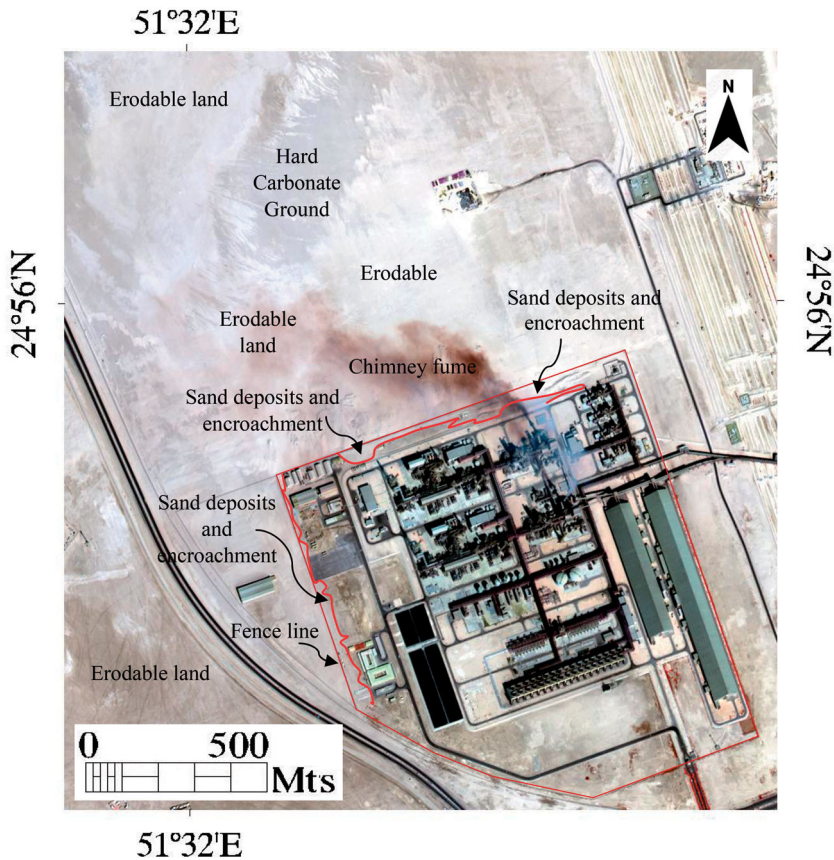


**Figure 6.** WorldView-2 satellite image showing the occurrence of sand deposits and encroachments near the fence and around the QAFCO site 5/6.

the occurrence and distribution of such dune deposits around the study region (Figure 2a in supplementary material). The dunes exhibited a maximum elevation of around 50 m. The hill-shaded image developed using the data indicated the windward sides of the dunes in bright and the leeward sides in the shades of gray (inset in Figure 2a in the supplementary material). Also, the interpretation of the direction of the predominant shamal wind over the State of Qatar (Bilal et al. 20121; Yu et al. 2016) represented that the wind prevails in the NW-SE direction (Figure 2b in supplementary material). The shamal wind could have influenced sand movement in the study region (Engel et al. 2018). In addition, the visual interpretation of WorldView-2 data (Figures 5 and 6) confirmed further the accumulation of high sand deposits and encroachments along the fences constructed on the northwest and southwest sides of the QAFCO site 5/6 when compared with the northeast and southeast sides of the site. The satellite images have the potential to show the regional distribution of sand deposits and dunes, and the deposits along the fence. The interpretation of images displayed the areas that are vulnerable to sand encroachment and land degradation.



**Figure 7.** Field photographs show (a) the occurrence of sand deposits (b) the sand dune (c) the fences (d) and (e) the encroachment of sand (f) to (i) the sand deposits over the pipeline, water trenches, metal roads (j) and (k) the sand deposit in the industry site (l) the damage of industry shed (m) to (q) the presence of vegetation, grasses and bushes and (r) and (s) the removing of sand deposits along the fences in and around the QAFCO site 5/6. Arrow indicates the direction of the north.

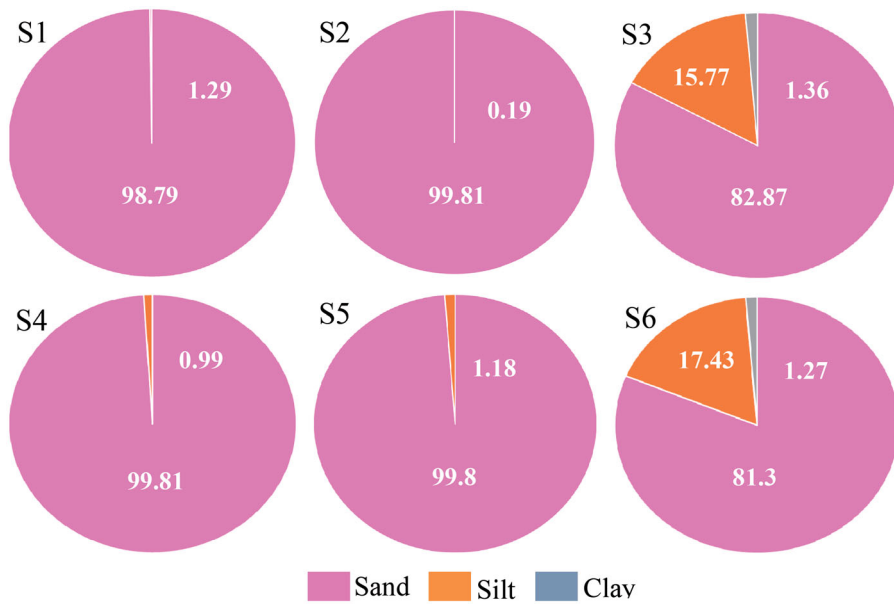


**Figure 8.** Distribution of sand, silt and clay in the sand deposits found in and around QAFCO site 5/6. Values are in percents.

**Table 2.** Distribution of sand, silt and clay in the samples collected in the QAFCO site 5/6.

Samples	Type	Sand	Silt	Clay
S1	Sand	98.79	1.21	0
S2	Sand	99.81	0.19	0
S3	Silty Sand	82.87	15.77	1.36
S4	Sand	99.01	0.99	0
S5	Sand	98.82	1.18	0
S6	Silty Sand	81.3	17.43	1.27

**Table 3.** Distribution of sand, silt and clay fractions in the sand samples collected in the QAFCO site 5/6.

Particle size distribution in %:	S1	S2	S3	S4	S5	S6
Clay (<4 $\mu\text{m}$ )	0	0	1.36	0	0	1.27
Silt (4–63 $\mu\text{m}$ )	1.21	0.19	15.77	0.99	1.18	17.43
Very fine sand (63–125 $\mu\text{m}$ )	4.65	4.64	9.28	7.65	6.37	6.52
Fine Sand (125–250 $\mu\text{m}$ )	62.43	76.11	53.67	76.09	79.8	41.02
Medium Sand (250–500 $\mu\text{m}$ )	29.89	19.02	19.69	15.27	12.65	28.04
Coarse sand (500–1000 $\mu\text{m}$ )	1.81	0.03	0.24	0	0	5.73
Very coarse sand (1000–2000 $\mu\text{m}$ )	0	0	0	0	0	0
Total Sand (63–2000 $\mu\text{m}$ )	98.79	99.81	82.88	99.01	98.82	81.3

### 4.3. Field and laboratory studies

#### 4.3.1. Field studies

The results of satellite data are checked and verified in the field by conducting field-work during May 2021. In the field, windblown sand deposits and dunes have occurred over carbonate rocks (Figure 7a). The occurrence of dunes in the southeast of the industry is observed (Figure 7b). The fences developed around the industry by



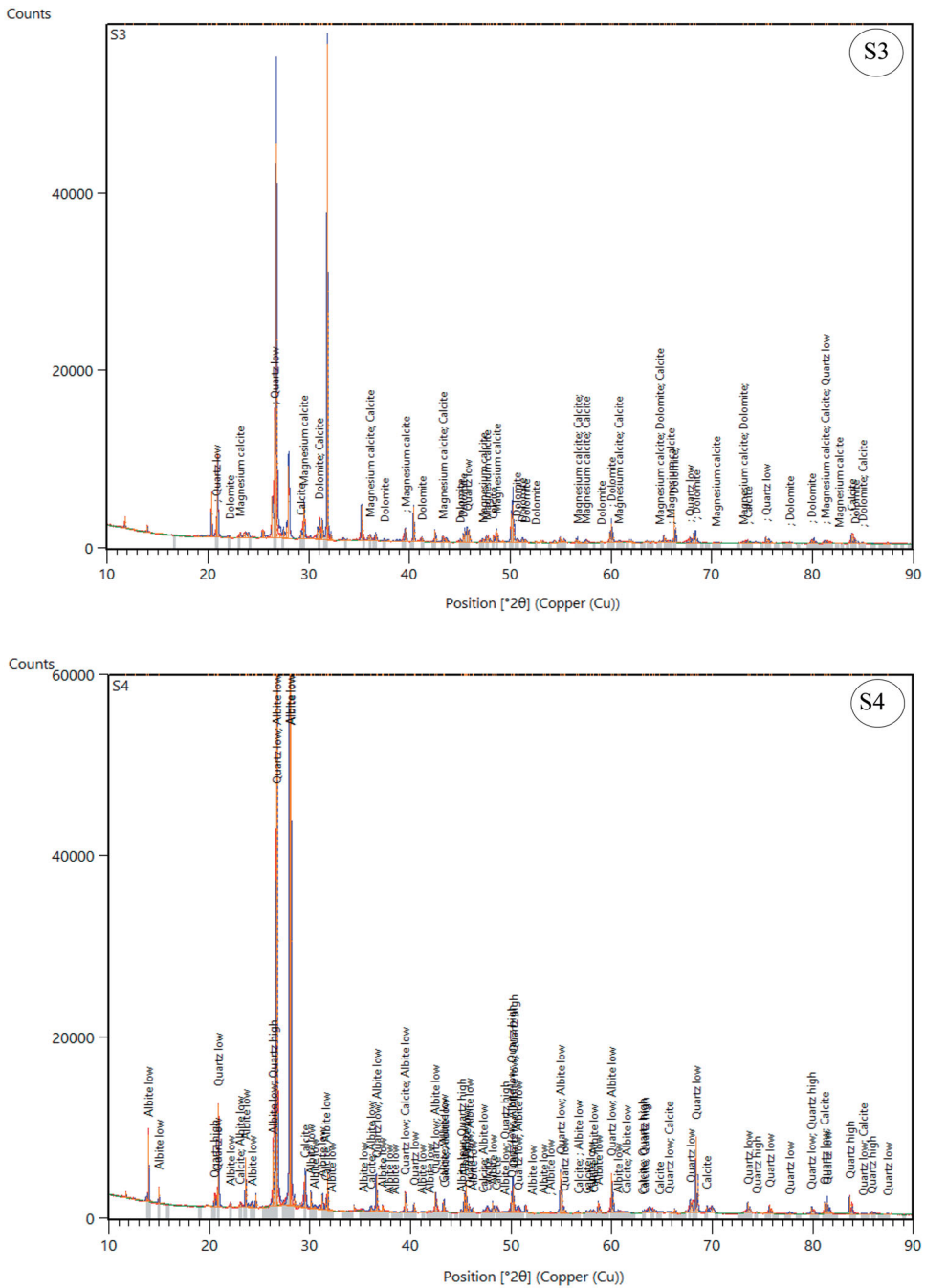


Figure 9. Continued.

and metalled roads, (Figure 7f–i), and deposited in the industry (Figure 7j and 7k). Corrosion in the infrastructure and damage to the industry shed due to windblown sand deposits were observed (Figure 7l). In the field, vegetation, grass, and bushes play a role in protecting and depositing the sand deposits (Figure 7m–q). As well, the

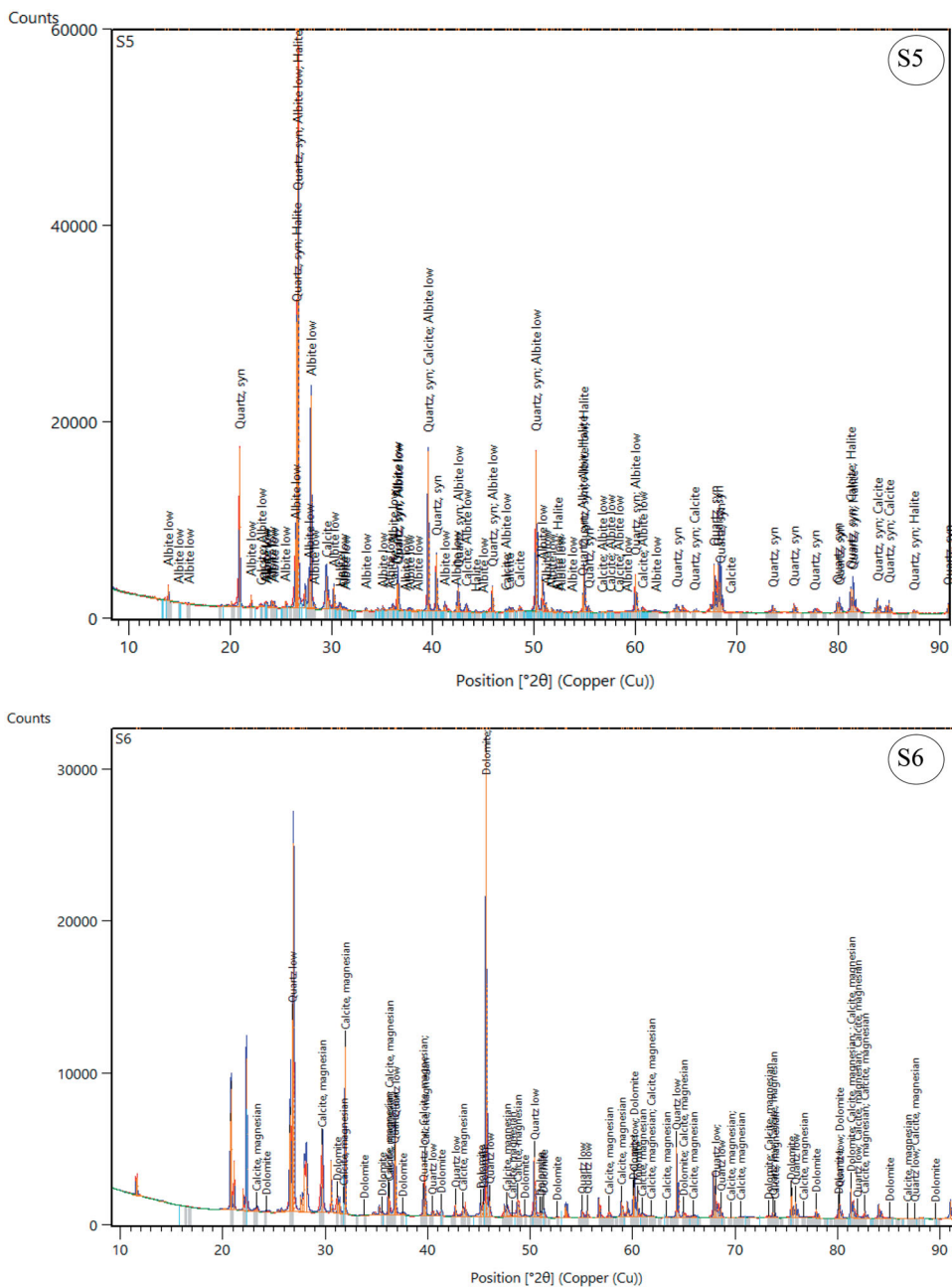


Figure 9. Continued.

removal of sand deposits along the fences, water trenches, and over the roads by QAFCO was observed (Figure 7h, 7r, and 7s). QAFCO waters the equipment and removes sand frequently for the maintenance of the industry. The field study confirmed the presence of sand deposits and sand encroachment and validated the remote sensing results.

**Table 4.** Distribution of major oxides in the samples of QAFCO site 5 and 6.

Elemental oxides in %	S1	S2	S3	S4	S5	S6
SiO <sub>2</sub>	27.7304	29.3086	25.3081	26.1424	76.7371	24.9230
Al <sub>2</sub> O <sub>3</sub>	4.8853	4.9889	3.7297	5.2308	5.6171	3.1127
MgO	1.8882	1.5909	2.7323	2.1238	1.9744	2.4687
CaO	11.7981	10.5440	10.7352	11.1712	10.3305	12.6915
FeO	0.6832	0.6166	0.7513	0.7644	0.7155	0.8322
Na <sub>2</sub> O	2.2470	2.6601	7.8862	4.1133	2.2842	4.4675
K <sub>2</sub> O	1.1850	0.1218	0.9026	1.1166	1.2133	0.8236
MnO	0.0172	0.0140	0.0166	0.0202	0.0160	0.0146
P <sub>2</sub> O <sub>5</sub>	0.0307	0.0310	0.0261	0.0322	0.0304	0.0260
Co <sub>3</sub>	29.17	26.87	39.76	30.74	25.33	42.27
Elements in ppm						
Sr	425.6	411.9	405.1	437.6	396.1	436.8
V	18.1	16.3	17.2	20.2	18.9	15.7
Cr	86.3	17.54	26.76	30.68	24.17	31.78
Cu	5.13	3.49	11.5	3.65	4.44	3.79
Ni	242.76	14	17.52	19.98	30.18	30.33
Pb	ND	0.01	7.73	0.63	ND	0.34
Zn	81.3	15.3	1124	24.2	105.5	25
B	2400.6	2338	2815.3	2339.6	2379.9	2225.5
Ba	244.1	248	189.9	240.6	257	191.4
Cd	ND	0.27	0.18	0.24	0.19	ND
Co	1.08	1.26	1.02	L9Z	1.75	0.87
Cl	13203.2	11629.3	49810.2	29949.4	6521.52	50049.1
SO <sub>4</sub>	2269.88	2116.17	5723.81	4675.86	4310.81	4291.14
PO <sub>4</sub>	0.12	0.16	0.12	0.12	0.15	0.12

**Table 5.** Arbitrary urease activity (AUA) and its specific production of isolates.

Isolate	Strain name	MALDI score	CFU (10 <sup>7</sup> cfu/mL)	Arbitrary urease activity (AUA/ mL)	Specific production (AUA/10 <sup>7</sup> cfu)
S1.1	<i>Providencia rettgeri</i>	2.47	6 ± 0.3	1.59 ± 0.1	2.9 ± 0.1
S1.2	<i>Bacillus cereus</i>	2.12	10 ± 1	3.92 ± 0.2	4.1 ± 0.2
S1.3	<i>Bacillus cereus</i>	2.05	6 ± 0.3	7.36 ± 0.4	12.7 ± 0.5
S1.4	<i>Bacillus cereus</i>	2.15	3 ± 0.1	3.55 ± 0.2	12.9 ± 0.3
S1.5	<i>Providencia rettgeri</i>	2.48	5 ± 0.2	9.65 ± 0.5	20.5 ± 0.8
S1.6	<i>Bacillus cereus</i>	2.14	39 ± 2	9.68 ± 0.5	2.5 ± 0.2
S3.2	<i>Providencia rettgeri</i>	2.37	20 ± 1	11.86 ± 0.6	5.9 ± 0.2
S3.3	<i>Bacillus subtilis</i>	2.11	9 ± 0.4	20.57 ± 1	23.6 ± 2.1
S3.4	<i>Bacillus subtilis</i>	1.96	5 ± 0.2	19.24 ± 1	39.3 ± 1.6
S5.3	<i>Providencia rettgeri</i>	2.45	7 ± 0.4	16.54 ± 0.8	22.3 ± 1.9

#### 4.3.2. Laboratory studies

The samples collected from the field (Table 1) were analyzed for grain sizes, mineralogy, and geochemical characteristics of the sand deposits. The results of grain size analyses of the samples indicated that the samples had predominantly sand grains (81.3 to 99.81%), a low amount of silt 0.19–17.43), and a very little amount of clay (1.27 to 1.36) (Figure 8; Table 2). The size fraction analyses of the sand represented that the samples had sand with sizes ranging from 125 to 500 µm, which is characteristic of fine to medium sand in distribution (Table 3; Figure 8). The plot drawn for the size classes confirmed that the deposits have unimodal sand distributions (Figure 3 in supplementary material). The XRD analyses of samples for identification of minerals confirmed the presence of quartz, calcite, magnesian calcite, dolomite, albite (quartz silicate), and halite minerals in the deposits (Figure 9).

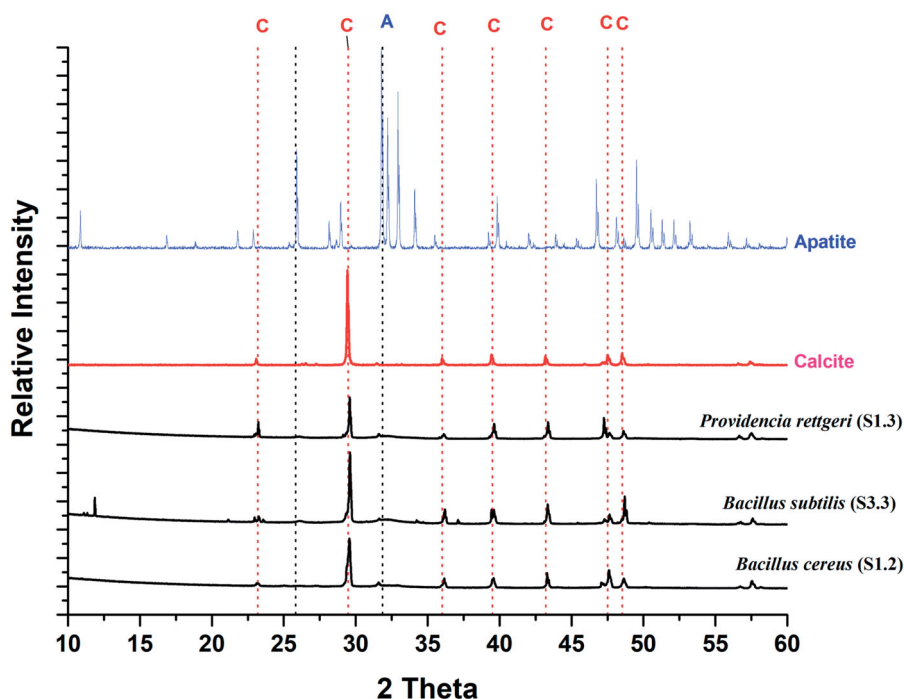


**Figure 10.** Representative XRD spectra showing mineral formed in the pure cultures of the studied bacterial strain (C—Calcite, A—Apatite).

The results of the analysis of samples for anion and cation concentrations are given in Table 4. The elemental analyses of samples indicated that the samples were rich in  $\text{SiO}_2$ ,  $\text{Al}_2\text{O}_3$ ,  $\text{CaO}$ ,  $\text{MgO}$ ,  $\text{Na}_2\text{O}$ ,  $\text{CO}_3$ ,  $\text{SO}_4$ ,  $\text{Cl}$ , and  $\text{B}$  and represent the presence of quartz and carbonate minerals in the samples. The presence of a high amount of  $\text{Al}_2\text{O}_3$  in the samples suggests the occurrence of silt and clay minerals in the deposits. As well, the presence of the high amount of  $\text{SO}_4$ ,  $\text{Cl}$ , and  $\text{B}$  in the samples represents the presence of gypsum ( $\text{CaSO}_4$ ) and halite salt ( $\text{NaCl}$ ) minerals in the samples and indicates that the samples have a mixture of sabkha soil in the coastal sediment environment.

## 5. Sand stabilization by bacteria method

During the sand stabilization study, 10 ureolytic bacteria strains were isolated and identified as 4 strains belonging to *Bacillus cereus* (S1.2, S1.3, S1.4, and S1.6), 2 strains of *Bacillus subtilis* (S3.3 and S3.4), and 4 strains of *Providencia rettgeri* (S1.1, S1.5, S3.2, and S5.5) species (Table 5, Figure 4 in supplementary material). The bacteria were stimulated well and formed mineral precipitation by producing urease enzyme, which catalyzed the hydrolysis of urea by forming  $\text{CO}_2$  and  $\text{NH}_3$ . The processes produced ammonia with high pH. The calcium ions in the soil matrix reacted with  $\text{CO}_2$  and formed calcium carbonate minerals which eventually bound the soil particles and improved the stabilization of soil under such alkaline conditions (Anbu et al. 2016; Krajewska 2018; Konstantinou et al. 2021). The high

specific activity in the formation of calcium carbonate is studied when cultured in the laboratory. The study of the bacterial communities isolated from the samples of the QAFCO site demonstrated the potential of several bacterial strains to produce urease enzymes.

The determination of urease activity indicated a high variation in the production of urease (Table 5). The bacterial strains *Bacillus subtilis* recorded the highest Specific production of urease activity as  $23.6 \pm 2.1$  and  $39.3 \pm 1.6$  AUA/ $10^7$  cfu in the samples S3.3 and S3.4 respectively. As well, *Providencia rettgeri* recorded  $22.3 \pm 1.9$  and  $20.5 \pm 0.8$  AUA/ $10^7$  cfu in the samples S5.3 and S1.5 respectively. Further, the analyses of minerals of the isolates by XRD represented the occurrence of calcium carbonate (Calcite) with calcium phosphates (Apatite) phases (Figure 10). The study of sand stabilization has shown the potential for stabilization at the sand of the QAFCO site and recommends applying infield to stop the erosion of deposits at the selected places of the site.

## 6. Conclusion

In this study, the characterization of the spectral emissive properties of quartz and carbonate minerals was described. The study of the spectral emissive properties of quartz minerals showed the presence of prominent spectral features due to fundamental asymmetric Si–O–Si stretching vibrations and the carbonate minerals have emissivity minima due to the C–O bending. The images developed using the TIR spectral bands of ASTER, and minerals indices displayed the presence of the quartz-rich sand deposits, dunes, and carbonate rock formations that occurred around the QAFCO site. The false-color composite (FCC) developed using the ASTER band 6, QI, and CI well discriminated the sand deposits and dunes in bright yellow and associated carbonate formations in a mixture of pink. The large-scale mapping of the site using the high spatial resolution data of WorldView-2 exhibited the presence of deposits and encroachments along the fences. The results of the satellite data are validated by field studies and analyses of field samples in the laboratory. The study confirmed the presence of sand deposits and sand encroachments along the fences. Plants, shrubs, and bushes play a vital role in protecting from erosion of sand deposits. The laboratory analyses of field samples indicated that the samples had predominantly sand grains and the presence of major minerals, namely quartz, calcite, magnesian calcite, dolomite, albite (quartz silicate), and halite minerals. The analyzes of samples for anion and cation concentration indicated a high concentration of  $\text{SiO}_2$ ,  $\text{Al}_2\text{O}_3$ ,  $\text{CaO}$ ,  $\text{MgO}$ ,  $\text{Na}_2\text{O}$ ,  $\text{CO}_3$ ,  $\text{SO}_4$ ,  $\text{Cl}$ , and  $\text{B}$  and represented the presence of quartz, silicate, and carbonate minerals. The presence of a high amount of  $\text{Al}_2\text{O}_3$  suggested the presence of silt and clay minerals and the concentrations of  $\text{SO}_4$ ,  $\text{Cl}$ , and  $\text{B}$  reflected the presence of gypsum ( $\text{CaSO}_4$ ) and halite salt ( $\text{NaCl}$ ) minerals in the sand deposits. The study of stabilization of sand demonstrated the stimulation of ureolytic bacteria and precipitation of minerals through MICP processes. The XRD analyses of the precipitates confirmed the presence of calcium carbonates (calcite) which would support sand stabilization methods at the QAFCO site.

## Acknowledgments

Open Access funding provided by the Qatar National Library. The authors are thankful to the NASA Land Processes Distributed Active Archive Center User Services, USGS Earth Resources Observation and Science (EROS) Center (<https://LPDAAC.usgs.gov>) for sharing the ASTER data, and the Digital Globe, USA is acknowledged for providing the WorldView-2 satellite image (Image ID: 104001004D7C7D00) that was acquired on February 16, 2021. Miss. Sarra Nejb Dimassi, Graduate Student (QU ID: 201510450), Qatar University, who obtained Research Assistantship from this project is thanked for her assistance in conducting the sand stabilization study. We are thankful to Mr. AbdulRahman Al-Sharif, Human Resources, QAFCO for his permission and support to conduct fieldwork at the QAFCO site 5/6. Mr. Mohammed Jaheer, Environmental Section, QAFCO, and Mr. Asim, F.S, Environmental Science Center are thanked for their help in conducting fieldwork. We thank Ms. J A Alnaimi H. A and her team at the Environmental Science Center for the laboratory analyses of samples. Mr. Abdulla Al Ashraf, CAM is thanked for the XRD analysis of samples. Ms. Aisha Begum and Ms. Sally Saliba, Environmental Science Center are thanked for the arrangement of permission to conduct fieldwork and manage this project study, respectively. The authors are thankful to Prof. Ramesh Singh, the Editor and anonymous reviewers of the journal for their valuable reviews, providing comments and suggestions that have helped to present the work lucidly.

## Disclosure statement

No potential conflict of interest was reported by the authors.

## Funding

This study is supported by Qatar University Grant no. QUEx-ESC-QAFCO-20/21-1.

## ORCID

Rajendran Sankaran  <http://orcid.org/0000-0002-9371-9908>

Fadhil N. Sadooni  <http://orcid.org/0000-0001-5027-0648>

Hamad Al-Saad Al-Kuwari  <http://orcid.org/0000-0001-6787-3533>

## Data availability statement

The data that support the findings of this study are available on request from the corresponding author.

## References

- Aboobacker VM, Samiksha SV, Veerasingam S, Al-Ansari MAS, Vethamony P. 2021. Role of shamal and easterly winds on the wave characteristics off Qatar, Central Arabian Gulf. *Ocean Eng.* 236:109457. <https://doi.org/10.1016/j.oceaneng.2021.109457>.
- Afrasinei GM, Melis MT, Arras C, Pistis M, Butta C, Ghiglieri G. 2018. Spatiotemporal and spectral analysis of sand encroachment dynamics in southern Tunisia. *Eur J Remote Sens.* 51(1):352–374. <https://doi.org/10.1080/22797254.2018.1439343>.

- Ahmady-Birgani H, McQueen KG, Moeinaddini M, Naseri H. 2017. Sand dune encroachment and desertification processes of the Rigboland sand sea, central Iran. *Sci Rep.* 7(1):1523. <https://doi.org/10.1038/s41598-017-01796-z>.
- Al-Disi ZA, Jaoua S, Al-Thani D, Al Meer S, Zouari N. 2016. Isolation, screening and activity of hydrocarbon-degrading bacteria from harsh soils. *Proceedings of the World Congress on Civil, Structural, and Environmental Engineering (CSEE'16), Prague, Czech Republic – March 30–31, 2016, Paper No. ICESDP 104.*
- Allbed A, Kumar L. 2013. Soil salinity mapping and monitoring in arid and semi-arid regions using remote sensing technology: a review. *ARS.* 02(04):373–385.
- Allbed A, Kumar L, Aldakheel YY. 2014a. Assessing soil salinity using soil salinity and vegetation indices derived from IKONOS high spatial resolution imageries: applications in a date palm dominated region. *Geoderma.* 230–231:1–8. <https://doi.org/10.1016/j.geoderma.2014.03.025>.
- Allbed A, Kumar L, Sinha P. 2014b. Mapping and modelling spatial variation in soil salinity in the Al Hassa Oasis based on remote sensing indicators and regression techniques. *Remote Sens.* 6(2):1137–1157. <https://doi.org/10.3390/rs6021137>.
- Amer R, Kusky TM, Ghulam A. 2010. Lithological mapping in the central-eastern desert of Egypt using ASTER data. *J Afr Earth Sci.* 56(2–3):75–82. <https://doi.org/10.1016/j.jafrearsci.2009.06.004>.
- Anbu P, Kang CH, Shin YJ, So JS. 2016. Formations of calcium carbonate minerals by bacteria and its multiple applications. *Springerplus.* 5:250. <https://doi.org/10.1186/s40064-016-1869-2>.
- Aydda A, Althuwaynee OF, Algouti A, Algouti A. 2019. Evolution of sand encroachment using supervised classification of Landsat data during the period 1987–2011 in a part of Laâyoune-Tarfaya basin of Morocco. *Geocarto Int.* 34(13):1514–1529. <https://doi.org/10.1080/10106049.2018.1493154>.
- Aydda A, Althuwaynee OF, Pokhare B. 2020. An easy method for barchan dunes automatic extraction from multispectral satellite data. *IOP Conf Ser: Earth Environ Sci.* 419(1):012015.
- Baird T, Bristow CS, Vermeesch P. 2019. Measuring sand dune migration rates with COSI-Corr and landsat: opportunities and challenges. *Remote Sens.* 11(20):2423. <https://doi.org/10.3390/rs11202423>.
- Bibi S, Oualha M, Ashfaq MY, Suleiman MT, Zouari N. 2018. Isolation, differentiation and biodiversity of ureolytic bacteria of Qatari soil and their potential in microbially induced calcite precipitation (MICP) for soil stabilization. *RSC Adv.* 8(11):5854–5863. <https://doi.org/10.1039/C7RA12758H>.
- Bilal H, Govindan R, Al-Ansari T. 2021. Investigation of groundwater depletion in the State of Qatar and its implication to energy water and food nexus. *Water.* 13(18):2464. <https://doi.org/10.3390/w13182464>.
- Bullard JE, White K. 2002. Quantifying iron oxide coatings on dune sands using spectrometric measurements: an example from the Simpson-Strzelecki Desert, Australia. *J Geophys Res.* 107(B6):ECV 5-1–ECV 5-11. <https://doi.org/10.1029/2001JB000454>.
- Burbank MB, Weaver TJ, Williams BC, Crawford RL. 2012. Urease activity of ureolytic bacteria isolated from six soils in which calcite was precipitated by indigenous bacteria. *Geomicrobiol J.* 29(4):389–395. <https://doi.org/10.1080/01490451.2011.575913>.
- Chavez PS, MacKinnon DJ. 1994. Automatic detection of vegetation changes in the southwestern United States using remotely sensed images. *Photogramm Eng Remote Sens.* 60: 571–583.
- Clark RN, King TVV, Klejwa M, Swayze GA, Vergo N. 1990. High spectral resolution reflectance spectroscopy of minerals. *J Geophys Res.* 95(B8):12653–12680. <https://doi.org/10.1029/JB095iB08p12653>.
- Corrie RK, Ninomiya Y, Aitchison JC. 2010. Applying advanced spaceborne thermal emission and reflection radiometer (ASTER) spectral indices for geological mapping and mineral identification on the Tibetan Plateau. *Int Arch Photogramm Remote Sens Spat Inf Sci.* XXXVIII(8):464–469.

- Crist EP, Cicone RC. 1984. Comparisons of the dimensionality and features of simulated Landsat-4 MSS and TM data. *Remote Sens Environ.* 14(1–3):235–246. [https://doi.org/10.1016/0034-4257\(84\)90018-X](https://doi.org/10.1016/0034-4257(84)90018-X).
- Crósta AP, De Souza Filho CR, Azevedo F, Brodie C. 2003. Targeting key alteration minerals in epithermal deposits in Patagonia, Argentina, using ASTER imagery and principal component analysis. *Int. J. Remote Sens.* 24(21):4233–4240. <https://doi.org/10.1080/0143116031000152291>.
- Cudahy T, Caccetta M, Thomas M, Hewson R, Abrams M, Kato M, Kashimura O, Ninomiya Y, Yamaguchi Y, Collings S, et al. 2016. Satellite-derived mineral mapping and monitoring of weathering, deposition and erosion. *Sci Rep.* 6(1):23702. <https://doi.org/10.1038/srep23702>.
- Delgado Blasco JM, Chini M, Verstraeten G, Hanssen RF. 2020. Sand dune dynamics exploiting a fully automatic method using satellite SAR data. *Remote Sens.* 12(23):3993. <https://doi.org/10.3390/rs12233993>.
- Eisele A, Chabrilat S, Hecker C, Hewson R, Lau IC, Rogass C, Segl K, Cudahy TJ, Udelhoven T, Hostert P, et al. 2015. Advantages using the thermal infrared (TIR) to detect and quantify semi-arid soil properties. *Remote Sens Environ.* 163:296–311. <https://doi.org/10.1016/j.rse.2015.04.001>.
- Engel M, Boesl F, Brückner H. 2018. Migration of barchan dunes in qatar—controls of the shama, teleconnections, sea-level changes and human impact. *Geosciences.* 8(7):240. <https://doi.org/10.3390/geosciences8070240>.
- Fichera CR, Modica G, Pollino M. 2012. Land cover classification and change detection analysis using multi-temporal remote sensed imagery and landscape metrics. *Eur J Remote Sens.* 45(1):1–18. <https://doi.org/10.5721/EuJRS20124501>.
- Fujisada H. 1995. Design and performance of ASTER instrument. *Proc SPIE Int Soc Opt Eng.* 2583:16–25. <https://doi.org/10.1117/12.228565>.
- Gabr S, Ghulam A, Kusky T. 2010. Detecting areas of high-potential gold mineralization using ASTER data. *Ore Geol Rev.* 38(1–2):59–69. <https://doi.org/10.1016/j.oregeorev.2010.05.007>.
- Gómez D, Salvador P, Sanz J, Casanova C, Casanova JL. 2018. Detecting areas vulnerable to sand encroachment using remote sensing and GIS techniques in Nouakchott, Mauritania. *Remote Sens.* 10(10):1541. <https://doi.org/10.3390/rs10101541>.
- Hamad AS. 2005. Lithostratigraphy of the Middle Eocene Dammam Formation in Qatar, Arabian Gulf: effects of sea-level fluctuations along a tidal environment. *J Asian Earth Sci.* 25:81–789. <https://doi.org/10.1016/j.jseaes.2004.07.009>.
- Hesse R. 2009. Using remote sensing to quantify aeolian transport and estimate the age of the terminal dune fields Dunas Pampa Blanca in southern Peru. *Quat Res.* 71(3):426–436. <https://doi.org/10.1016/j.yqres.2009.02.002>.
- Hogland J, Billor N, Anderson N. 2013. Comparison of standard maximum likelihood classification and polytomous logistic regression used in remote sensing. *Eur J Remote Sens.* 46(1):623–640. <https://doi.org/10.5721/EuJRS20134637>.
- Hook SJ, Gabell AR, Green AA, Kealy PS. 1992. A comparison of techniques for extracting emissivity information from thermal infrared data for geologic studies. *Remote Sens Environ.* 42(2):123–135. [https://doi.org/10.1016/0034-4257\(92\)90096-3](https://doi.org/10.1016/0034-4257(92)90096-3).
- Hughenoltz CH, Levin N, Barchyn TE, Baddock MC. 2012. Remote sensing and spatial analysis of aeolian sand dunes: a review and outlook. *Earth Sci. Rev.* 111(3–4):319–334. <https://doi.org/10.1016/j.earscirev.2011.11.006>.
- Hunt GR. 1977. Spectral signatures of particulate minerals in the visible and near-infrared. *Geophysics.* 42(3):501–513. <https://doi.org/10.1190/1.1440721>.
- Hunt GR, Salisbury JW. 1974. Mid-infrared spectral behavior of igneous rocks. Technical report AFRCL-TR-75-0356. US Air Force Cambridge Research Laboratory, Cambridge.
- Hunt GR, Salisbury JW. 1975. Mid-infrared spectral behavior of sedimentary rocks. Technical report AFRCL-TR-75-0356. US Air Force Cambridge Research Laboratory, Cambridge.

- Hunt GR, Salisbury JW. 1976. Mid-infrared spectral behavior of metamorphic rocks, Technical Report AFRCL-TR-76-0003. US Air Force Cambridge Research Laboratory, Cambridge.
- Hunt GR, Salisbury JW, Lenhof CJ. 1973. Visible and near-infrared spectra of minerals and rocks. VI. Additional silicates. *Modern Geol.* 4:85–106.
- Julien Y, Sobrino JA, Jiménez-Muñoz JC. 2011. Land use classification from multitemporal Landsat imagery using the Yearly Land Cover Dynamics (YLCD) method. *Int J Appl Earth Obs Geoinf.* 13(5):711–720. <https://doi.org/10.1016/j.jag.2011.05.008>.
- Karanisa T, Amato A, Richer R, Abdul Majid S, Skelhorn C, Sayadi S. 2021. Agricultural production in Qatar's hot arid climate. *Sustainability.* 13(7):4059. <https://doi.org/10.3390/su13074059>.
- Knipling EB. 1970. Physical and physiological basis for the reflectance of visible and near-infrared radiation from vegetation. *Remote Sens Environ.* 1(3):155–159. [https://doi.org/10.1016/S0034-4257\(70\)80021-9](https://doi.org/10.1016/S0034-4257(70)80021-9).
- Konstantinou C, Wang Y, Biscontin G, Soga K. 2021. The role of bacterial urease activity on the uniformity of carbonate precipitation profiles of bio-treated coarse sand specimens. *Sci Rep.* 11(1):6161. <https://doi.org/10.1038/s41598-021-85712-6>.
- Krajewska B. 2018. Urease-aided calcium carbonate mineralization for engineering applications: a review. *J Adv Res.* 13:59–67. <https://doi.org/10.1016/j.jare.2017.10.009>.
- Levin N, Kidron GJ, Ben-Dor E. 2006. The spatial and temporal variability of sand erosion across a stabilizing coastal dune field. *Sedimentology.* 53(4):697–715. <https://doi.org/10.1111/j.1365-3091.2006.00787.x>.
- Li XR, Kong DS, Tan HJ, Wang XP. 2007. Changes in soil and vegetation following stabilization of dunes in the southeastern fringe of the Tengger Desert. *Plant Soil.* 300(1–2): 221–231. [10.1007/s11104-007-9407-1](https://doi.org/10.1007/s11104-007-9407-1).
- Li XR, Zhang JG, Wang XP. 2000. Study on microbiotic crust and its influences on sand fixing vegetation in arid desert region. *Acta Bot Sin.* 42:965–970.
- Li XR, Zhou HY, Wang XP, Zhu YG, O'Conner PJ. 2003. The effects of sand stabilization and revegetation on cryptogam species diversity and soil fertility in the Tengger Desert, Northern China. *Plant Soil.* 251(2):237–245. <https://doi.org/10.1023/A:1023023702248>.
- Ninomiya Y. 2002. Mapping quartz, carbonate minerals and mafic-ultramafic rocks using remotely sensed multispectral thermal infrared ASTER data. *Proc SPIE.* 4710:191–202. <https://doi.org/10.1117/12.459566>.
- Ninomiya Y, Fu B. 2003. Extracting lithologic information from ASTER multispectral thermal infrared data in the northeastern Pamirs. *Xinjiang Geol.* 21(1):22–29.
- Ninomiya Y, Fu B, Cudahy TJ. 2005. Detecting lithology with advanced spaceborne thermal emission and reflection radiometer (ASTER) multispectral thermal infrared “radiance-at-sensor” data. *Remote Sens Environ.* 99(1–2):127–139. <https://doi.org/10.1016/j.rse.2005.06.009>.
- Notaro M, Yu Y, Kalashnikova OV. 2015. Regime shift in Arabian dust activity, triggered by persistent Fertile Crescent drought. *J Geophys Res Atmos.* 120(19):229–210, 249.
- Peng Y, Kheir RB, Adhikari K, Malinowski R, Greve MB, Knadel M, Greve MH. 2016. Digital mapping of toxic metals in Qatari soils using remote sensing and ancillary data. *Remote Sens.* 8(12):1003.
- Pradhan B, Moneir A, Jena R. 2018. Sand dune risk assessment in Sabha region, Libya using Landsat 8, MODIS, and Google Earth Engine images. *Geomat Nat Hazards Risk.* 9(1): 1280–1305.
- Qiu H, Cui Y, Hu S, Yang D, Pei Y, Ma S, Liu Z. 2019. Size distribution and size of loess slides in response to slope height and slope gradient based on field survey data. *Geomat Nat Hazards Risk.* 10(1):1443–1458.
- Rajendran S, Hersi OS, Al-Harthy AR, Al-Wardi M, El-Ghali MA, Al-Abri AH. 2011. Capability of Advanced Spaceborne Thermal Emission and Reflection Radiometer (ASTER) on discrimination of Carbonates and associated rocks and Mineral Identification of Eastern

- Mountain region (Saih Hatat Window) of Sultanate of Oman. Carbonates Evaporites. 26(4): 351–364. <https://doi.org/10.1007/s13146-011-0071-4>.
- Rajendran S, Nasir S, Al Jabri K. 2020. Mapping and accuracy assessment of siltation of recharge dams using remote sensing technique. *Sci Rep.* 10(1):10364. <https://doi.org/10.1038/s41598-020-67137-9>.
- Rockwell BW, Hofstra AH. 2008. Identification of quartz and carbonate minerals across northern Nevada using ASTER thermal infrared emissivity data—Implications for geologic mapping and mineral resource investigations in well-studied and frontier areas. *Geosphere.* 4(1): 218–246. <https://doi.org/10.1130/GES00126.1>.
- Rowan LC, Hook SJ, Abrams MJ, Mars JC. 2003. Mapping hydrothermally altered rocks at the Cuprite Nevada using the advanced space-borne thermal emission and reflection radiometer (ASTER), a new satellite-imaging system. *Econ. Geol.* 98(5):1019–1027. <https://doi.org/10.2113/gsecongeo.98.5.1019>.
- Rowan LC, Kingston MJ, Crowley JK. 1986. Spectral reflectance of carbonatite and related alkalic igneous rocks from four North American localities. *Econ. Geol.* 81(4):857–871. <https://doi.org/10.2113/gsecongeo.81.4.857>.
- Runnström MC. 2003. Rangeland development of the Mu Us Sandy Land in semiarid China: an analysis using Landsat and NOAA remote sensing data. *Land Degrad Dev.* 14(2): 189–202. <http://dx.doi.org/10.1002/ldr.545/>.
- Song Q, Gao X, Lei J, Li S. 2019. Spatial distribution of sand dunes and their relationship with fluvial systems on the southern margin of the Taklimakan Desert, China. *Geomat Nat Hazards Risk.* 10(1):2408–2428.
- Sur K, Chauhan P. 2019. Imaging spectroscopic approach for land degradation studies: a case study from the arid land of India. *Geomat Nat Hazards Risk.* 10(1):898–911.
- Vacca A, Loddo S, Melis MT, Funedda A, Puddu R, Verona M, Fanni S, Fantola F, Madrau S, Marrone VA, et al. 2014. A GIS based method for soil mapping in Sardinia, Italy: a geomatic approach. *J Environ Manage.* 138:87–96. <https://doi.org/10.1016/j.jenvman.2013.11.018>.
- Vaughan RG, Calvin WM, Taranik JV. 2003. SEBASS hyperspectral thermal infrared data: surface emissivity measurement and mineral mapping. *Remote Sens Environ.* 85(1):48–63. [https://doi.org/10.1016/S0034-4257\(02\)00186-4](https://doi.org/10.1016/S0034-4257(02)00186-4).
- Vogiatzakis IN, Melis MT. 2015. Changing perceptions in Mediterranean Geography: the role of geospatial tools. In Douguédroit A, Theano LFC, Terkenli S, Editors. *Connections, mobilities, urban prospects and environmental threats. The Mediterranean transition.* Newcastle upon Tyne, UK: Cambridge Scholars Publishing.
- Wang X, Tao J, Bao R, Tran T, Tucker-Kulesza S. 2018. Surficial soil stabilization against water-induced erosion using polymer-modified microbially induced carbonate precipitation. *J Mater Civ Eng.* 30(10):04018267.
- Weiner S, Dove PM. 2003. An overview of biomineralization processes and the problems of the vital effect. *Rev Mineral Geochem.* 54(1):1–29. <https://doi.org/10.2113/0540001>.
- Wen Y, Guo B, Zang W, Ge D, Luo W, Zhao H. 2020. Desertification detection model in Naiman Banner based on the albedo-modified soil adjusted vegetation index feature space using the Landsat8 OLI images. *Geomat Nat Hazards Risk.* 11(1):544–558.
- Wolfe SA, Hugenholz CH. 2009. Barchan dunes stabilized under recent climate warming on the northern Great Plains. *Geology.* 37(11):1039–1042. <https://doi.org/10.1130/G30334A.1>.
- Xu Z, Li Z, Liu H, Zhang X, Hao Q, Cui Y, Yang S, Liu M, Wang H, Gielen G, et al. 2018. Soil organic carbon in particle-size fractions under three grassland types in Inner Mongolia, China. *J Soils Sediments.* 18(5):1896–1905. <https://doi.org/10.1007/s11368-018-1951-1>.
- Yamaguchi Y, Naito C. 2003. Spectral indices for lithologic discrimination and mapping by using the ASTER SWIR bands. *Int J Remote Sens.* 24(22):4311–4323. <https://doi.org/10.1080/01431160110070320>.

- Yu Y, Notaro M, Kalashnikova OV, Garay MJ. 2016. Climatology of summer Shamal wind in the Middle East. *J Geophys Res Atmos.* 121(1):289–305.
- Zhang H, Yin A, Yang X, Wu P, Fan M, Wu J, Zhang M, Gao C. 2019. Changes in surface soil organic/inorganic carbon concentrations and their driving forces in reclaimed coastal tidal flats. *Geoderma.* 352:150–159. <https://doi.org/10.1016/j.geoderma.2019.06.003>.
- Zhang Z-S, Li X-R, Nowak RS, Wu P, Gao Y-H, Zhao Y, Huang L, Hu Y-G, Jia R-L. 2013. Effect of sand-stabilizing shrubs on soil respiration in a temperate desert. *Plant Soil.* 367(1–2):449–463.
- Zhao Y, Gao X, Lei J, Li S, Song Q, Zhou N. 2019. Interactions between paleochannels and aeolian processes and their implications on aeolian dune patterns. *Geomat Nat Hazards Risk.* 10(1):1176–1192.